Prediction of a compressible flow through a 3D channel by Large Eddy Simulation with the mixed scale model

L. Coquart, C. Tenaud, L. Ta Phuoc

LIMSI - CNRS, UPR 3251, BP 133, 91403 Orsay Cedex, FRANCE

Abstract

This study deals with the Large Eddy Simulation (LES) of an unsteady turbulent compressible internal flow at high Reynolds number, in sight of turbomachinery applications. To validate the subgrid scale modeling near the walls when shock-waves and shock-waves/boundary layers interaction occur, the simulation of the flow in a 3D transonic convergent-divergent channel (ONERA) is performed. This test case is very well documented since it has already been studied experimentally [6] and numerically with RANS modeling [7], [27]. The experimental results and RANS simulations are compared with the results given by the mixed scale model using a WENO shock capturing scheme [48] of third order.

1 Introduction

Unsteady flows produced in unadapted turbomachinery are characterized by diverse unsteady phenomena that involves the diminution of the pressure recovery of the industrial machines. Shock wave/turbulence or shock wave/boundary layer interactions can be observed in the turbomachinery flows or in the air intake of the aircrafts in unadapted flow conditions. It can lead to important propulsion or compression performance losses. The unsteady 3D shock wave/boundary layer interaction that can occur in these transonic flows remains one of the main issue that has to be studied in detail at high Reynolds number. The shock wave, by interacting with the turbulent flow, can lead to high fluctuations in wall pressure as well as strong unsteady heat flux. When a separation occurs, large unsteady energetic recirculations are created. These unsteady large scale structures can significantly increase the loads on the different solid structures. The low frequency contraction and expansion of the separation zone induces the large scale oscillation of the shock/wave. The turbulent coherent stuctures also produce pressure fluctuations at higher frequency by interacting with the shock wave [32], [44]. The unsteady shock wave/boundary layer interaction that takes place in these flows is very complex and still not very well understood and controlled. On the opposite of the flows encountered in the air intake of the aircrafts, turbomachinery flows are characterized by a rotating movement. As a matter of fact, three different origins to turbomachinery flows unsteadiness can be distinguished.

The first one is the rotation of the blade row which produce a periodic motion at relatively low frequency. Opiela and al. realized a **LES** (**L**arge **E**ddy **S**imulation) to study the interation between a turbulent wake flow, generated by a periodically moving

cylinder, and a stator blade [43]. It appears that the passing of the wake causes temporary separation on the suction side of the blade. J. M. Verdon, in [54], studied the response of the steady flow passing through a blade row to an harmonic perturbation at the frequency of ω. The results indicate propagating acoustic responses at the inlet and at the exit of the row.
The second origin of the flow unsteadiness is related to the motion of the paddle wheels, as it happens for example in a shock-wave/boundary layer interaction with separation. The paddle wheels are excited by the pressure fluctuations of the recirculation. This unsteady motion generates waves that interact, in a non linear way, back with the flow. Carstens and Schmitt have shown that the nonlinear fluid structure interaction, caused by oscillating shocks or strong flow separation, can significantly influence the intrinsic wheel motion [9]. Some methods with coupled aerodynamics and structural models have also been used, as did Sadeghi and Liu [46] who solved the aerodynamical and structural equations simultaneously. The study reveals that the intrinsic oscillatory modes of the wheels are not amplified in the same way than in the uncoupled approach.
Then, the third origin of unsteadiness in turbomachinery flows is turbulence itself, and the interaction of the large energetic anisotropic eddies of the flow with the shock-wave. This study, performed in collaboration with the Industry Research Consortium in Turbomachinery (CIRT) and the LEMFI (Orsay), deals more precisely with the calculation of the large anisotropic eddies encountered in these kind of flows and with the turbulence modeling, in the presence of a shock wave/boundary layer interaction.

The resolution of the full turbulent compressible Navier-Stokes equations with a **RANS** (**R**eynolds **A**verage **N**avier **S**tokes equations) approach, by using an algebraic mixing length turbulence model, or using a $k-\varepsilon$ turbulence model, are now commonly used to simulate industrial flows and particularly turbomachinery flows [6], [10], [29]. Anyway, these models can present some shortcomings in the capture of the phenomena experimentally observed in shock/wave boundary layer interactions. K. Hanjalić lists the advantages and the limits of the two equation eddy viscosity models in [49], as does P. R. Spalart in [30]. It was observed, for example, that very large separation zone, in a flow where a shock wave/boundary layer interaction occurs, was overestimated by these methods [27]. Recently, more and more complex $R_{ij}-\varepsilon$ turbulence closure models were developed to improve the prediction of the flow/solid structure interactions and the turbulence properties. The resolution of the Reynolds stress components allow to take into account the anisotropy of turbulence. This kind of modelization improves the calculation of the separation, as shown by M. A. Leschziner and al., in their simulation of a shock wave/boundary layer interaction [36].

The **RANS** $k-\varepsilon$ and $R_{ij}-\varepsilon$ turbulence models, initially constructed for high $\mathcal{R}e$ number, were extended to near wall low Reynolds flow in the nineties [27]. Several modified models are reviewed by R. M. C. So and al. in [45]. It can be underline that one of the difficulty is to modelize the pressure redistribution term Φ_{ij}. Also, the models have to be asymptotically coherent with the turbulence near wall feature. These low $\mathcal{R}e$ number models give better results than the usual models, but they are still complex and computationnally expansive. T. J. Craft, in [15], and G. A. Gerolymos in [28], proposed a low Reynolds closure adapted for the simulation of the near wall flow region but in-

dependant of the geometric parameters, as the distance from the wall. This simplifies the use of second order moment closures in 3D complex geometries, like those encountered in turbomachinery flows. Non linear viscosity $k - \varepsilon$ models were also proposed by Leschziner and al., [36], as a compromise between the classical eddy viscosity models and the second order closures. The **R**enormalization **G**roup (**RNG**) theory of V. Yakhot and L. M. Smith, [57], is another promising research direction, with a new theoritical support.

All the methods discussed above are intrinsically steady predicitive. Unsteady simulations are performed thanks to URANS modelization [48]. This approach is constructed upon a phase average and actually only give unsteady predictions of the flow motion when the separation between the predominant unsteady phenomenon frequency and the turbulence frequencies is well-defined. P. R. Spalart has also proposed an hybrid methodology called **DES** (**D**etached **E**ddy **V**iscosity) [48]. It consists of using a RANS model to calculate the boundary layer, coupled to a Large Eddy Simulation in the separated regions of the flow. The method gives good results in the simulation of a flow past a circular cylinder and will have to be extended for the simulation of internal flows.

One of the weakness of the RANS approach is that all the scales are modeled. They hardly correctly resolved the large unsteady energetic structures. $R_{ij} - \varepsilon$ closures describe more faithfully the turbulence dynamics, but they are still complex and steady predictive. The aim of this work is then to validate the **LES** (**L**arge **E**ddy **S**imulation) modeling of a shock wave/boundary layer interaction with the mixed scale model [50], in sight of turbomachinery applications.

In the **LES** approach, the large energetic scales filtered from the global field by the computational grid mesh size locally, are resolved. The small scales, unresolved through the local mesh, are modeled. LES subgrid modeling has already been used successfully to simulate external turbulent unsteady flows. F. Ducros and al. [11], [20], simulated the transition to turbulence in a boundary layer developing spatially over a flat plate. C. Tenaud and L. Ta Phuoc compared different LES closure models for the simulation of the unsteady compressible separated flow around NACA airfoil [50]. B. Vreman and al. have simulated a compressible plane mixing layer to test the LES subgrid contribution of the modelized terms [55]. The LES of spatially developing 3D compressible mixing layer has been also realized with the mixed scale model by L. Doris and al. [19]. Different subgrid models were compared recently in the simulation of a turbulent jet wake/vortex interaction by C. Ferreira Gago and al. in [23]. Thermal effects were also studied in their configuration.

LES of internal flow in a channel have also been performed. P. Moin and J. Kim analyzed in detail the mean velocity profiles and the turbulence statistics in turbulent channel flow at $\mathcal{R}e = 13800$ [41]. E. Lenormand and al. tested different subgrid models for LES of compressible wall bounded flows in a periodical channel [34]. C. Brun and R. Friedrich performed a priori tests of subgrid stress models in a fully developed pipe flow by reconstructing the small scale tensor from their DNS (**D**irect **N**umerical **S**imulation) [5]. R. Verzicco and al., in [54], calculated the incompressible flow in a motored axisymmetric pistion-cylinder assembly by LES. The boundary conditions were applied independently of the grid by using body forces. X. Wu and P. A. Durbin performed a DNS of an

incompressible flow passing through turbine passages to study the rotor wakes/stator interactions [56].

The simulation of compressible flow through complex geometries thanks to the LES approach is more recent. As already mentionned, M. Opiela and al. performed a LES to simulate the interaction between a wake generated by a moving cylinder and the stator in a turbine stage in a compressible flow [42]. Several studies on the shock-wave/boundary layer interactions in supersonic flows can be founded in the literature. Rizzeta and al. studied the flow structure and the turbulence properties thanks to a LES of a supersonic compression ramp flow at $M = 3$ and $\mathcal{R}e = 2.1\ 10^4$ [16]. H. Yan and D. Knight, in [58], have performed a LES of a supersonic compression corner at $M = 2.88$ and $\mathcal{R}e = 10^4$. N. A. Adams also performed a DNS of the turbulent boundary layer along a compression ramp at $M = 3$ and $\mathcal{R}e = 1685$ [1].

These kind of flows and phenomena have been less investigated in the transonic regime [25]. The turbulent unsteady compressible flow through a 3D channel (ONERA), with a swept bump on the lower wall, is simulated, at high Reynolds number. This corresponds to the "Delery's Case C", a classic test case for investigating turbulence-model performance for shock wave/boundary layer interaction [36]. Multiple shock-wave/boundary layer interactions take place on the four walls, and a large 3D separation can be experimentally observed downstream of the bump. Detailed experiments are available, as well as statistical simlulations, making possible the validation of the LES through a comparison between numerical and experimental results [6], [27]. The 3D shock wave/boundary layer interaction that takes place tends to mimic patterns occuring in an unadapted flow over the blades, even if the rotation of the flow is not taken into account in this study. The flow presents some of the main characteristics of the flows encountered in turbomachinery, specially in supersonic or transonic axial compressors. The objective of the present paper is to analyze in detail the large scale field calculated by LES in a three dimensional shock-wave/boundary layer interaction occuring in an internal turbulent transonic flow. The simulation is performed using the mixed scale model [50] and with a third order WENO shock capturing scheme [32].

The test case is described in the next section. LES governing equations with the terms that have been modeled are presented, as well as the subgrid mixed-scale model. The numerical resolution of the equations, the description of the tested numerical scheme and the boundary conditions are given. The unsteady results obtained by LES are discussed. Some temporal spectra, made downstream from the interaction zone, are analized. Then, the different results obtained by LES are compared to the results given experimentally and by statistical methods on the mean velocity profiles and the Reynolds stress tensor, to specify if the main average properties of the flow are recovered with the LES subgrid modeling.

2 Tested configuration : the 3D ONERA Channel

The tested configuration is a 3D channel (ONERA) with a swept bump on the lower wall. It has been studied numerically by RANS approach [7], [29] and experimentally in a wind tunnel at ONERA [6]. The geometrical definition of the configuration is presented in figure (1). The total length of the channel is $L_x = 0.8$ m, the test section at the inlet is $L_y = 0.1$ m high and $L_z = 0.1213$ m wide. As we can see in figure (1), the throat is obtained by the bump with 3D shape located on the flow of this channel. The upstream part of the bump is straight and is inclined at 7 degrees. Then the surface of the swept bump is circular. The first portion is concave with a radius of 0.1 m, followed by a convex part characterized by a 0.18 m radius of curvature. The construction of the bump insures the slope continuity of the two circular parts. The bump crest line is swept of 30 degrees from the inflow direction [6]. The chord length of the bump varies from $\chi = 0.245\ m$ on the far side wall, to $\chi = 0.355\ m$ on the near side wall. The height of the bump is 0.02 m. The channel has a second throat, visible in figure (1) close to the end, which its cross section is adjustable to allow a very precise location of the shock wave produced in the channel. The coordinate origin $x = 0$ m is located at the beginning of the bump, so x varies from $x = -0.1$ m to $x = 0.7$ m along the computational domain. The coordinate $z = 0$ m corresponds to the farest lateral wall and $y = 0$ m coincides with the lower wall at the inlet.

This configuration has been defined at ONERA and studied experimentally in the S8 transonic wind tunnel. The reservoir pressure and temperature of the air in the experience, were $P_t = 0.92\ 10^5$ Pa and $T_t = 300$ K. The Reynolds number based on both the minimum chord length of the bump, $\chi = 0.245$ m, and the maximum inlet velocity, $u_{ref} = 198\ m\ s^{-1}$, is $\mathcal{R}e = 22\ 10^5$.

The incoming flow is subsonic with a maximum Mach number $M = 0.6$ in the core of the flow. The flow accelerates on the bump reaching a sonic state in the first throat at the maximum height of the bump. A three dimensional shock wave takes place downstream the bump [6], [39]. Its location in the divergent part depends on the opening of the second sonic throat. The simulation of this throat in the definition of the tested case geometry is necessary, as the pressure is not homogeneous in the outflow [7], [27]. The streamwise location of the second throat is the same as in the experiments. In the RANS simulation, the opening of the throat is adjusted to recover the experimental shock wave location in the divergent. The shock wave interacts with the boundary layer on the upper and the lower wall. On the lower wall, on the far side, the pressure in the boundary layer is higher than the pressure downstream of the shock wave, and the boundary layer does not separate. On the nearest side wall, the shock-wave/boundary layer interaction intensity is strong enough to generate a large dead-water region [27]. The flow is then reaccelerated in the divergent part downstream the shock wave. It becomes sonic in the second throat and the core of the outflow is supersonic.

The measured data consist of profiles of the velocity components and the Reynolds stress tensor components along the (Ox), (Oy), and (Oz) axes. Only the experimental profiles along the (Oy) direction were compared to the numerical results, at seven different abscissa x, centered in the separation zone, and at five different coordinates z. The field

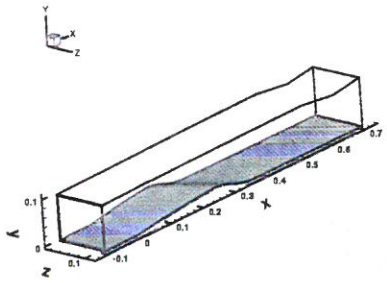

Figure 1: Sketch of the 3D ONERA Channel : computational domain

measurements were executed by using a three-component laser Doppler velocimeter. The expected accuracy given by the experimentalists is 1% for the velocity components u_i, while it is of order of 10% for $u'v'$ and 20% for $v'w'$.

3 LES Governing Equations and Subgrid Modelling

3.1 Filtered equations

The governing equations of the compressible turbulent flow are the unsteady Navier-Stokes equations. In LES, the fields are decomposed into a spatially resolved part and a subgrid-scale part. For convenience, in a compressible flow, the resolved variables are density-weighted [22] and are then given by :

$$f = \widetilde{f} + f'' \text{ with } \widetilde{f} = \overline{\rho f}/\overline{\rho}.$$

$\overline{(.)}$ is the spatial filtering operator. $\widetilde{f}$, the Favre's variable, is the resolved part of the quantity. The spatial filtering operation is implicit. The characteristic filter size depens on the local grid size and the numerical scheme intrinsic dissipation. In the above decomposition, f'' pictures the unresolved density-weighted subgrid-scale part which is uncaptured through the mesh used.

The filtered Navier-Stokes equations can be written in different ways [34]. More unresolved terms appear in the compressible filtered equations than in the incompressible ones. Following Vreman [55], the equations are written with only resolved quantities but without introducing modified energy, temperature or pressure. In the simulation, the temperature and the pressure are resolved quantities and the subgrid contributions appearing in the total energy are modeled separately. As we compare our numerical results to experimental ones, it is necessary to simulate a real pressure. Anyway, a recent review upon the use of a macro temperature and a macro pressure to simulate a flow through a channel [38], concludes that the subgrid contribution to pressure and temperature is negligible under a reasonable subgrid mach number condition.

Our equations are close to one of the system proposed by Vreman in [55]. The weight of the different subgrid terms appearing in the filtered equations are compared to each other in [55] thanks to the simulation of the temporal development of a mixing layer. The results lead to the conclusion that all the subgrid terms can be neglected, except the

non-linear subgrid-scale tensor, the subgrid-scale heat flux and the threefold correlations $\frac{\rho}{2}(u_i\widetilde{u_i}u_j - \widetilde{u_i}\widetilde{u_i}\widetilde{u_j})$. We neglect, a priori, the contribution of the threefold correlations, while the subgrid-scale tensor, the subgrid-scale heat flux and the contributions in the total energy are modeled. The possible modelization of $\frac{\rho}{2}(u_i\widetilde{u_i}u_j - \widetilde{u_i}\widetilde{u_i}\widetilde{u_j})$, for instance using a first gradient hypothesis [34], has to be first validated in a simpler test case than the Delery's case. This was not planned in the initial frame of this study. We can underline that the hypothesis used in our simulation were apply successfully to the LES of a spatially developing 3D compressible mixing layer [19].

Finally, the governing equations of the large scale motion are written, in Cartesian coordinate, as :

$$\overline{\frac{\partial Q}{\partial t}} + \overline{\frac{\partial F}{\partial x}} + \overline{\frac{\partial G}{\partial y}} + \overline{\frac{\partial H}{\partial z}} - \overline{\frac{\partial F_v}{\partial x}} - \overline{\frac{\partial G_v}{\partial y}} - \overline{\frac{\partial H_v}{\partial z}} = 0$$

with

$$\overline{Q} = \begin{pmatrix} \overline{\rho} \\ \overline{\rho}\widetilde{u} \\ \overline{\rho}\widetilde{v} \\ \overline{\rho}\widetilde{w} \\ \overline{\rho}\widetilde{E} \end{pmatrix} \qquad \overline{F} = \begin{pmatrix} \overline{\rho}\widetilde{u} \\ \overline{\rho}\widetilde{u}^2 + \overline{p} \\ \overline{\rho}\widetilde{u}\widetilde{v} \\ \overline{\rho}\widetilde{u}\widetilde{w} \\ \overline{\rho}\widetilde{u}\widetilde{E} + \widetilde{u}\overline{p} \end{pmatrix} \qquad \overline{G} = \begin{pmatrix} \overline{\rho}\widetilde{v} \\ \overline{\rho}\widetilde{u}\widetilde{v} \\ \overline{\rho}\widetilde{v}^2 + \overline{p} \\ \overline{\rho}\widetilde{v}\widetilde{w} \\ \overline{\rho}\widetilde{v}\widetilde{E} + \widetilde{v}\overline{p} \end{pmatrix} \qquad \overline{H} = \begin{pmatrix} \overline{\rho}\widetilde{w} \\ \overline{\rho}\widetilde{u}\widetilde{w} \\ \overline{\rho}\widetilde{v}\widetilde{w} \\ \overline{\rho}\widetilde{w}^2 + \overline{p} \\ \overline{\rho}\widetilde{w}\widetilde{E} + \widetilde{w}\overline{p} \end{pmatrix}$$

$$\overline{F_v} = \begin{pmatrix} 0 \\ \widetilde{\sigma}_{11} + \tau_{11} \\ \widetilde{\sigma}_{12} + \tau_{12} \\ \widetilde{\sigma}_{13} + \tau_{13} \\ \widetilde{u}(\widetilde{\sigma}_{11} + \tau_{11}) + \widetilde{v}(\widetilde{\sigma}_{12} + \tau_{12}) + \widetilde{w}(\widetilde{\sigma}_{13} + \tau_{13}) - q_1 - \psi_1 \end{pmatrix}$$

$$\overline{G_v} = \begin{pmatrix} 0 \\ \widetilde{\sigma}_{12} + \tau_{12} \\ \widetilde{\sigma}_{22} + \tau_{22} \\ \widetilde{\sigma}_{23} + \tau_{23} \\ \widetilde{u}(\widetilde{\sigma}_{12} + \tau_{12}) + \widetilde{v}(\widetilde{\sigma}_{22} + \tau_{22}) + \widetilde{w}(\widetilde{\sigma}_{23} + \tau_{23}) - q_2 - \psi_2 \end{pmatrix}$$

$$\overline{H_v} = \begin{pmatrix} 0 \\ \widetilde{\sigma}_{13} + \tau_{13} \\ \widetilde{\sigma}_{23} + \tau_{23} \\ \widetilde{\sigma}_{33} + \tau_{33} \\ \widetilde{u}(\widetilde{\sigma}_{13} + \tau_{13}) + \widetilde{v}(\widetilde{\sigma}_{23} + \tau_{23}) + \widetilde{w}(\widetilde{\sigma}_{33} + \tau_{33}) - q_3 - \psi_3 \end{pmatrix}$$

Both operators appearing in the fluxes, $\widetilde{(.)}$ and $\overline{(.)}$, correspond to resolved quantities in connection with the spatial filtering. Then, in terms of large scales, $\overline{\rho}$ is the density of the fluid, $\widetilde{u}_i$ is the velocity component in the x_i direction, $\overline{p}$ is the pressure, $\widetilde{E}$ is the total energy and $\widetilde{q}_j$ is the heat fux vector. $\widetilde{\sigma}_{ij}$ is the viscous stress tensor of the re-

solved velocity : $\tilde{\sigma}_{ij} = 2\mu(\tilde{S}_{ij} - \frac{1}{3}\tilde{S}_{kk}\delta_{ij})$ where μ is the dynamic viscosity. Let us recall that μ is given by the Sutherland's law : $\mu(\tilde{T}) = \mu(T_o)\ (\frac{\tilde{T}}{T_o})^{\frac{3}{2}}\ \frac{T_o + 110.4}{\tilde{T} + 110.4}$. The quantity $\tilde{S}_{ij} = \frac{1}{2}(\frac{\partial \tilde{u}_i}{\partial x_j} + \frac{\partial \tilde{u}_j}{\partial x_i})$ is the strain rate tensor of the resolved velocity. The heat flux vector is given by the Fourier's law : $\tilde{q}_j = -\kappa \frac{\partial \tilde{T}}{\partial x_j}$, where κ is the thermal conductivity given by $\kappa = \frac{\mu\ c_p}{Pr}$. The air flow simulated is supposed to behave like a perfect gas so $Pr = 0.7$ and the thermodynamic pressure is calculated from the ideal gas equation state : $\overline{p} = \overline{\rho}\mathcal{R}\tilde{T} = (\gamma - 1)\ \overline{\rho}\ (\tilde{E} - \frac{\widetilde{u_i u_i}}{2})$ with $\gamma = 1.4$ and $\mathcal{R} = 287\ J/kg\ K$.

$\tau_{ij} = \overline{\rho}(\widetilde{u_i u_j} - \tilde{u}_i \tilde{u}_j)$ is the subgrid stress tensor and $\psi_j = (c_p \overline{\rho}(\widetilde{u_j T} - \tilde{u}_j \tilde{T}))$ is the subgrid heat flux. These two terms need to be related to the resolved quantities by the use of models which are listed below. As already pointed out, the subgrid kinetic energy contribution, τ_{kk}, is needed in the evaluation of the temperature and the pressure. A similarity scale assumption is employed to estimate τ_{kk} [50]. However, as shown in [38], this contribution is not essential.

As the geometry of the nozzle is not cartesian, the equations are resolved in a curvilinear coordinate system (ξ, η, ζ) that fits the 3D channel [51]. The velocity components, still expressed in the cartesian coordinates, are functions of (ξ, η, ζ). The $\xi(x, y, z)$ coordinate defines the longitudinal direction. The $\eta(x, y, z)$ coordinate is locally normal to the surfaces following the lower wall up to the upper wall. The third coordinate $\zeta(x, y, z)$ is normal to the side wall planes.

Finally we resolve :

$$J\frac{\partial \overline{Q}}{\partial t} + \frac{\partial \widehat{F}}{\partial \xi} + \frac{\partial \widehat{G}}{\partial \eta} + \frac{\partial \widehat{H}}{\partial \zeta} - \frac{\partial \widehat{F_v}}{\partial \xi} - \frac{\partial \widehat{G_v}}{\partial \eta} - \frac{\partial \widehat{H_v}}{\partial \zeta} = 0 \tag{1}$$

with

$$\widehat{F} = \alpha_\xi \overline{F} + \beta_\xi \overline{G} + \gamma_\xi \overline{H}\ ,\ \widehat{G} = \alpha_\eta \overline{F} + \beta_\eta \overline{G} + \gamma_\eta \overline{H}\ ,\ \widehat{H} = \alpha_\zeta \overline{F} + \beta_\zeta \overline{G} + \gamma_\zeta \overline{H}$$

$$\widehat{F_v} = \alpha_\xi \overline{F_v} + \beta_\xi \overline{G_v} + \gamma_\xi \overline{H_v}\ ,\ \widehat{G_v} = \alpha_\eta \overline{F_v} + \beta_\eta \overline{G_v} + \gamma_\eta \overline{H_v}\ ,\ \widehat{H_v} = \alpha_\zeta \overline{F_v} + \beta_\zeta \overline{G_v} + \gamma_\zeta \overline{H_v}$$

J is the jacobian of the transformation and α_i, β_j et γ_k are the local metric of the coordinates transformation [31].

3.2 Subgrid modeling

Following the energy transfert theory, the subgrid stress tensor is evaluated by a Boussinesq hypothesis. In this approach, the deviatoric part of the subgrid scale tensor is related to the strain rate tensor of the resolved velocity field by means of a subgrid viscosity as :

$$-\tau_{ij} + \frac{1}{3}\tau_{kk}\delta_{ij} = 2\ \mu_{sg}\ (\widetilde{S_{ij}} - \frac{1}{3}\widetilde{S_{kk}}\delta_{ij})$$

The subgrid viscosity, μ_{sg}, is modeled by the mixed scale model adapted to compressible flow [50]. The mixed modelization was prefered to a dynamical approach [26] because the dynamic model can present undesirable numerical oscillations. It is also a model computationally more expansive than the mixed scale model [24]. LES of test-case at high Reynolds number were also already performed successfully for external flows with the mixed scale model, as the simulation of a 3D spatial mixing layer [19] or the simulation of a compressible jet [23].

In this model, the subgrid viscosity μ_{sg} is defined as the geometric ponderation between the vorticity model and the kinetic energy model [3] :

$$\mu_{sg} = (\underbrace{\overline{\rho}\, C_s^2\, \Delta^2\, |\overline{\omega}|}_{\mu_\omega}\ \underbrace{\overline{\rho}\, C_b\, \Delta\, \sqrt{q_c}}_{\mu_k})^{\frac{1}{2}}$$

The vorticity model, constructed upon the large scales, is used to calculate μ_ω [2]. $C_s^2 = 0.04$ and Δ is the cut off length scale of the filter. The vorticity model has been prefered to the Smagorinsky model because the constant value is less sensible to the local shear stress in the fluid [3]. This is important here as the flow simulated is bounded, with strong velocity gradients at the wall. The turbulent kinetic energy model [3], based upon the unresolved scales, evaluates the small scale contribution of the viscosity μ_k. $C_b = 0.126$ and q_c is the subgrid kinetic energy at the cut off, given by a scale similarity assumption as : $q_c = \frac{1}{2}\,(\widetilde{u_i})''(\widetilde{u_i})'' = \frac{1}{2}\,(\widetilde{u_i} - \breve{\widetilde{u_i}})(\widetilde{u_i} - \breve{\widetilde{u_i}})$. The double-filtered quantities $\breve{\widetilde{u_i}}$ are computed by using a filter with a cut off of 2Δ. To end with, and to be consistent with the subgrid kinetic energy modeling, τ_{kk} is approximated by $2\overline{\rho}q_c$.

We can underline that with this kind of mixed modelization, the effect of both scales is balanced. Also, the viscosity goes to zero in a laminar zone, near the walls, or where the flow is well resolved. The viscosity induced by the model is less important than the Smagorinsky's one, as the value of the global viscosity changes with the amount of small scales present in the local spatial spectrum of the flow quantities, at the filter's cut off [33].

The subgrid heat flux is modeled by a first gradient formulation :

$$\psi_j = -\kappa_{sg}\frac{\partial \widetilde{T}}{\partial x_j}$$

Under the assumption of a Reynolds analogy, the subgrid thermal conductivity, κ_{sg}, is evaluated from the subgrid viscosity in a similar way than the molecular thermal conductivity. The dynamical heat transfert process is supposed to follow the dynamical kinetic process. The subgrid thermal conductivity is then evaluated by using a constant subgrid Prantl number assumption [11] : $\kappa_{sg} = \frac{\mu_{sg} C_p}{Pr_{sg}}$ with $Pr_{sg} = 0.6$. It did not seem necessary to use yet a more complex modeling for κ_{sg} in this simulation, as for instance a temperature-velocity correlations closure [46].

4 Numerical Resolution

Time integration of the equations is decoupled from spatial discretization. The discretization is entirely explicit and the global scheme is stable under an usual CFL and diffusion

like condition. In the following, a discreet variable estimated at a grid point $\xi_i = i$, $\eta_j = j$, $\zeta_k = k$ and at the time level $t = n\ \Delta t$ is referred as $(.)^n_{i,j,k}$. Even if the velocity components are still expressed in the cartesian coordinates system, the derivatives appearing in the system of equations (1) are evaluated in the new curvilinear coordinates (ξ, η, ζ). In this system, the points are spatially equidistant and $\Delta\xi = \Delta\eta = \Delta\zeta = 1$.

4.1 Time integration

The time discretization is perfomed by a third order, total variation diminishing (TVD), Runge-Kutta scheme [47]. The resolution of the equations in time is then given by :

$$\begin{aligned}
\overline{Q}^{(1)} &= \overline{Q}^{(0)} + \Delta t\ L(\overline{Q}^{(0)}) \\
\overline{Q}^{(2)} &= \frac{3}{4}\overline{Q}^{(0)} + \frac{1}{4}\overline{Q}^{(1)} + \frac{1}{4}\Delta t\ L(\overline{Q}^{(1)}) \qquad \text{where} \qquad \overline{Q}^{(0)} = \overline{Q}^{(n)} \text{ and } \overline{Q}^{(3)} = \overline{Q}^{(n+1)} \\
\overline{Q}^{(3)} &= \frac{1}{3}\overline{Q}^{(0)} + \frac{2}{3}\overline{Q}^{(2)} + \frac{2}{3}\Delta t\ L(\overline{Q}^{(2)})
\end{aligned}$$

This prediction-projection scheme is well adapted to unsteady flow. The operator $L(Q)$, appearing in the temporal scheme represents the TVD spatial operator with the discretized convective and diffusive terms.

4.2 Spatial discretization

The convective terms $\widehat{F}$, $\widehat{G}$, $\widehat{H}$, and the diffusive terms $\widehat{F_v}$, $\widehat{G_v}$, $\widehat{H_v}$ are discretized separately. Convective terms are discretized by using a third order WENO scheme, and diffusive terms with a second order centered scheme. In compressible LES, it is necessary to use high order shock capturing schemes to evaluate the discreet Euler fluxes, as the intrinsic numerical dissipation introduced by the scheme is in competition with the dissipation of the subgrid scale model. It is also important to have the best perfomances as possible on the recent vectorial computers. We only present the spatial discretization of the nonlinear convective fluxes, as the discreet form of the viscous fluxes is trivial. The convective terms are written in the conservative form as :

$$\frac{\partial \widehat{F}}{\partial \xi} + \frac{\partial \widehat{G}}{\partial \eta} + \frac{\partial \widehat{H}}{\partial \zeta} = \left(\frac{\check{F}^n_{i+1/2,j,k} - \check{F}^n_{i-1/2,j,k}}{\Delta\xi}\right) + \left(\frac{\check{G}^n_{i,j+1/2,k} - \check{G}^n_{i,j-1/2,k}}{\Delta\eta}\right) + \left(\frac{\check{H}^n_{i,j,k+1/2} - \check{H}^n_{i,j,k-1/2}}{\Delta\zeta}\right)$$

The convective fluxes are calculated with the WENO scheme based on the work of G.S. Jiang and C.W. Shu [32], [40]. The WENO scheme is a weighted combination of solutions constructed upon each r available stencil of the ENO reconstruction, by polynomial interpolation. The generic ENO scheme selects the stencil on which the solution calculated numerically is the most regular. Then the weight associated to each reconstruction is a function of the regularity of the solution. The authors introduce a new smoothness measurement of the regularity of the numerical solution on a stencil r, by minimizing the L^2 norm derivatives of the solution. Then the rth-order of the usual ENO scheme can be improved up to $(2r-1)$th-order in the smooth regions.

C_l^r	$l=0$	$l=1$	$l=2$
$r=2$	1/3	2/3	
$r=3$	1/10	6/10	3/10

Table 1: Coefficients C_l^r for $r=3$

As we use a Roe scheme, based upon the local caracteristic variables, the fluxes are evaluated as a function of the sign of the eigenvalues. When the eigenvalue, λ_m, is positive, the fluxes are given by their value at the right side of the interface $x_{i+1/2,j,k}$ and are written as :

$$(\check{F}^m_{i+1/2,j,k})_{WENO} = \sum_{l=0}^{r-1} \omega_l^m (q_l^r(\widehat{F}_{i+l-r+1,j,k}, ..., \widehat{F}_{i+l,j,k}))_{ENO} \qquad \lambda_m \geq 0$$

Otherwise, $(\check{F}^m_{i+1/2,j,k})_{WENO}$ is calculated by its expression on the left side :

$$(\check{F}^m_{i+1/2,j,k})_{WENO} = \sum_{l=0}^{r-1} \omega_l^m (q_{l+1}^r(\widehat{F}_{i+l-r+2,j,k}, ..., \widehat{F}_{i+l+1,j,k}))_{ENO} \qquad \lambda_m \leq 0$$

$q_l^r(\widehat{F}_{i+l-r+1,j,k}, ..., \widehat{F}_{i+l,j,k})$ are the ENO reconstructed fluxes up to the order r on the stencil S_l [49]. The variables ω_l^m are the weights assign to each candidate stencil S_l :

$$\sum_{l=0}^{r-1} \omega_l = 1 \quad ; \quad \omega_l = \frac{\beta_l}{\beta_0 + \beta_1 + ... + \beta_{r-1}} \quad ; \quad \beta_l = \frac{C_l^r}{(\varepsilon + IS_l)^2}$$

$\varepsilon \simeq 10^{-6}$ avoids the denominator beeing zero. IS_l measures the smoothness of the flux on a stencil l. As already said it is calculated from the L^2 norm of all the derivatives of the interpolation polynomial [32]. The C_l^r coefficients are calculated to ensure the $(2r-1)$th-order in the smooth regions. They are given in the Table (1) [4], [32].

The reconstruction is performed along the characteristic direction, by projecting the Euler fluxes onto the left eigenvector matrices $R^{-1}_{i+1/2,j,k}$ of $(A_\xi)_{i+1/2,j,k} = (\frac{\partial \widehat{F}}{\partial Q})_{i+1/2,j,k}$. The expression of the numerical fluxes are finally obtained by projecting back, into the physical space, the reconstructed fluxes onto the right eigenvectors $R_{i+1/2,j,k}$:

$$(\check{F}_{i+1/2,j,k})_{WENO} = \sum_{m=1}^{5} [\sum_{l=0}^{r-1} \omega_l^m (\sum_{p=0}^{r-1} \delta_{l,p}^r R^{-1,m}_{i+1/2,j,k}.\widehat{F}(Q_{i+l+p-r+1,j,k}) R^m_{i+1/2,j,k})]$$

where $\delta_{l,p}^r$ are the ENO polynomial interpolation coefficient given in the Table (2) [32].

4.3 Computational Domain, Initial and Boundary conditions

The figure (2) represents the computational domain. The volume explored experimentally with a three-component laser Doppler velocimeter [6] is limited by the planes $x = 0.230$ m and $x = 0.390$ m, as visible in figure (2).

r	l	$p=0$	$p=1$	$p=2$
3	0	1/3	−7/6	11/6
	1	−1/6	5/6	1/3
	2	1/3	5/6	−1/6
	3	11/6	−7/6	1/3

Table 2: Coefficients $\delta^r_{l,p}$ for $r = 3$

The computational domain has respectivelly $401 \times 151 \times 101$ grid points, in the three directions of space. The grid mesh used with the WENO scheme has twice more points in the longitudinal direction than the RANS's one. There are also more points in the vertical direction than RANS.
The three distributions of the mesh spacing in wall unit $dx_p^+ = \Delta x(\frac{\rho}{\mu}\sqrt{\frac{\tau_p}{\mu}})_{wall}$, dy_p^+ and dz_p^+, are represented in the figure (3). dx_p^+ is plotted against the variable i at $y = 0.04m$ and $z = 0.112m$. In the interaction zone, $250 < dx_p^+ < 100$. The strong variation of dx_p^+ observed around $i = 180$ corresponds to the end of the interaction zone. The variables dy_p^+ and dz_p^+ are plotted at five different stations x. $x = 0.09m$ is upstream of the shock-wave/boundary layer interaction and $x = 0.496m$ is downstream of the recirculation zone. The mesh spacing along (Oy) is bounded by $100 < dy_p^+ < 300$, while $150 < dz_p^+ < 400$.

A statistical converged flow field, calculated with the Launder-Shima $R_{ij} - \varepsilon$ turbulence modeling [27], is prescribed as an initial solution in the entire computational domain.

No slip conditions are imposed at the four wall that are supposed insulated. The fifth imposed equation is the continuity equation, resolved at the wall by upwinding differences [17].

At the subsonic inlet, the mean temperature $\langle\tilde{T}\rangle$, the mean flow rate $\langle\rho\tilde{u}\rangle$, the mean vertical and cross velocity components, $\langle\tilde{v}\rangle$ and $\langle\tilde{w}\rangle$, are prescribed. They are calculated from the initial statistical field. The unsteadiness of the flow is obtained by superimposing, at the inlet, a spatially white noise to the spanwise velocity components, v'' and w''. The white noise is generated by a random function in space but deterministic in time. On the contrary of a RANS simulation where all the scales are time average, a LES corresponds to one realization of the flow field in time. It is then important to reproduce in time the evolution of the random function to compare two realizations. As the inlet flow is subsonic, the pressure is calculated with the caracteristic equation associated to the negative eigenvalue $(\langle\tilde{u}\rangle - c)$ using a non reflective condition [12], [52].

At the outlet, the flow is supersonic in the core because of the second throat. The equations are projected onto the characteristic directions in the supersonic part of the flow. A non reflective boundary condition is prescribed in the boundary layers where the eigenvalue $(\langle\tilde{u}\rangle - c)$ is negative.

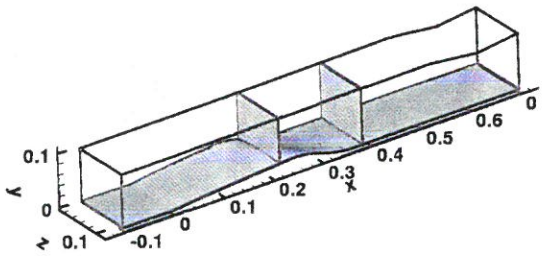

Figure 2: Computational domain and volume explored experimentally

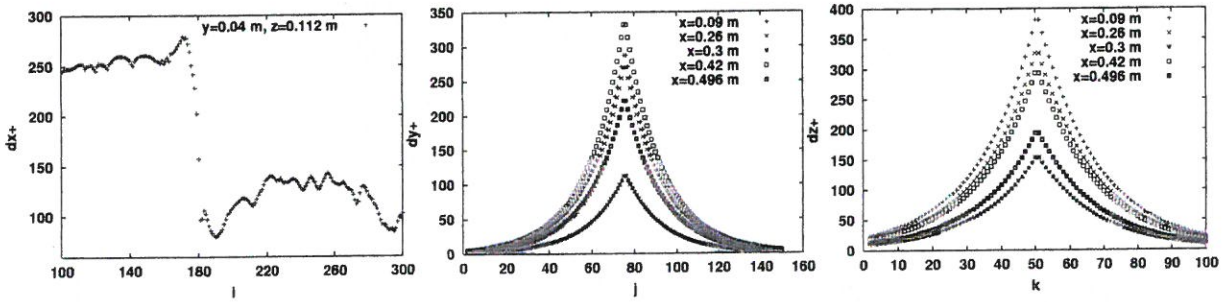

Figure 3: Distribution of the mesh spacing dx^+, dy^+, dz^+ in wall units along $0.1 \leq x \leq 0.5$ ($100 \leq i \leq 300$), (Oy) and (Oz) respectively

5 Numerical Results

The different grid mesh characteristics used for the LES and the RANS simulations [27], to which our numerical results are compared, are summarized up in Table (3). As already mentioned, we compare our results both to the experiments of Delery at ONERA [6] and to RANS results obtained by means of the Launder-Shima model.

Case	N_x	N_y	N_z	y_p^+	z_p^+	CFL
LES simulation	401	151	101	9	40	0,73
RANS simulation	201	91	101	0.75	0.75	50

Table 3: Characteristics of the grid mesh

y_p^+ and z_p^+ characterize the maximum coordinates in wall units of the first grid point over the walls, in the vertical and spanwise directions. The CFL used in the RANS simulation is much higher than in the LES simulation, since the RANS time integration have been performed by means of an implicit algorithm.

In the presentation of our results, the reference length is the minimum chord length of the bump $\chi = 0.245$ m. The reference velocity is the inlet maximum velocity $u_{ref} = 198\ m\ s^{-1}$. Then the reference time is given by : $t_{ref} = \dfrac{\chi}{u_{ref}} = 1.225\ 10^{-3}$ s.

The simulation has been performed on a parallel NEC-SX5 computer (IDRIS-CNRS),

by using 4 processors. The CPU time is close to 10^{-6} (sec/point/time step) and the code reaches about 3.5 Gflops.

5.1 Data processing

All the notations used in the presentation of the numerical results, as well as the obtaining of the numerical data to plot the different profiles are summarized up below.

In the following, $\langle q \rangle$ is a time average quantity. Then $\widehat{q} = \dfrac{\langle \rho q \rangle}{\langle \rho \rangle}$ is the resolved part in the Favre temporal decomposition : $q = \widehat{q} + q'''$ and q''' is the unresolved density-weighted time scale contribution. As already defined, $\overline{q}$ is a spatial filtered quantity and $\widetilde{q} = \dfrac{\overline{\rho q}}{\overline{\rho}}$ is the corresponding density-weighted Favre's variable. We have $q = \widetilde{q} + q''$, with q'' the spatially density-weighted unresolved contribution. Some spectra have been realized downstream of the 3D interaction and $q' = \widetilde{q} - \langle \widetilde{q} \rangle$ pictures the fluctuations in time of the spatially resolved quantities. All the subgrid contributions have been neglected in the evaluation of the time average of the velocity and the Reynolds stress components in the LES results. Also, all the velocities are made dimensionless by the inlet reference velocity u_{ref} and the Reynolds stress tensor components by u_{ref}^2. Their profiles along (Oy) are compared to the components measured experimentally and simulated with RANS. As the RANS variables are density weighted, the data are compared to $\widehat{u_i}$ which is evaluated by $\widehat{u_i} = \dfrac{\langle \overline{\rho} \widetilde{u_i} \rangle}{\langle \overline{\rho} \rangle}$. The Reynolds stress tensor components are calculated by

$$\widehat{u_i''' u_j'''} = \frac{\langle \overline{\rho} \widetilde{u_i} \widetilde{u_j} \rangle}{\langle \overline{\rho} \rangle} - \frac{(\langle \overline{\rho} \widetilde{u_i} \rangle)(\langle \overline{\rho} \widetilde{u_j} \rangle)}{(\langle \overline{\rho} \rangle)^2}$$

The snapshots of the unsteady results presented in figures (4b), (5b) and (6b) are the spatially resolved velocity components obtained at the dimensionless time of $t^* = 5.69$.

The sampling of data, used to realize the spectra of w' downstream of the interaction, figure (9), has been performed during $\Delta t^* = 1.26$, from $t^* = 0.735$.

Finally, the time storage of the spatially resolved velocity and Reynolds stress tensor components data has been also realized during $\Delta t^* = 2.84$, at the end of the simulation. These quantities are presented figure (10) to figure (20).

5.2 Unsteady results

One of the objectives of the LES methodology is the prediction of the large anisotropic structures created in the recirculations resulting from the shock waves/boundary layers interaction. The unsteady results obtained by LES in a small longitudinal portion of the flow, downstream of the bump, in the 3D interaction, are then discussed.

The three initial velocity components are presented respectively in figure (4a), (5a) and (6a) in a (x, y) plane where the boundary layer separates. The dead water region is visible below the lambda shape like shock pattern in figure (4a). Following the description in [27], the Launder-Shima statistical $R_{ij} - \varepsilon$ model overpredicts the extent of this dead water zone. Yet this is one of the main cornerstone of the modeling. The main characteristic here of the 3D shock-wave/boundary layer interaction is the strong reinjection of fluid in

the recirculation in the spanwise direction. This phenomenon can be explained by the conjugate effects of the interaction and the 3D deflected shape of the bump. The wrong recovery of this strong injection in the statistical modeling induces the too large extent of the separation.

The three unsteady velocity components obtained by LES are presented in figure (4b), (5b) and (6b) in the same (x, y) plane as the initial ones. The creation of turbulent eddies, convected by the mean flow, has been observed with the LES simulation. The recirculation zone is visible below the shock wave in figure (4a). The high shear layer in this region of interaction develops an instability which, in return has certainly an impact on the shock wave. Some vortices are ejected in time. The mechanism of creation of this high shear layer is explained thanks to the sketch of the fondamental interaction between a shock wave and a boundary layer in 2D in figure (7). The boundary layer separates when the pressure behind the shock wave is stronger than the pressure in the boundary layer. Then if the recirculation is entirely supersonic, a lambda-shape like shock pattern is created [40]. The separated "bubble" that takes place under the lambda-shape like shock pattern is delimited by a supersonic shear layer. This is a region of strong gradients and some instabilities take place in the shear layer leading to the creation of turbulent eddies [17]. This mechanism explains the presence of structures visible on the vertical and spanwise velocity components, figures (5b) and (6b).

The figure (4b) presents the longitudinal unsteady velocity component obtained by the LES. The fluid reaccelerates downstream of the shock-wave/boundary layer interaction. The large ejected structures modify the detached boundary layer thickness along (Ox) which induces a virtual variable section in the core of the flow. This leads to the generation of the multiple shock-wave pattern [8] with sonic points, observed in the divergent part of the channel in figure (4b). As the boundary layer is thicker, the flow rate is smaller in the core and the fluid is locally accelerated in the upper part of the channel.

The figure (5b) represents the unsteady vertical velocity component. A succession of shock waves propagate in the divergent. Positive and negative vertical velocity component value, that alternate in the boundary layers downstream of the interaction, characterize the presence of vortices.

This can be also observed in figure (6b) where the spanwise velocity component is plotted. The locally positive zone below a local negative zone, in figure (6b), characterizes the presence of unsteady longitudinal rollups downstream of the bump. A large negative zone is visible in both figures (6a) and (6b), around $x = 0.3$ m. It correponds to the deviation of the fluid to the left side wall because of the dissymetry of the bump. The fluid is then injected downstream of the bump in the dead water region. This is characterized by the positive value of $\tilde{w}$ near the lower wall in the separation in figure (6a). This is also visible in figure (6b) where the injection is stronger and more localized in the LES results than in RANS results.

These unsteady LES results are very encouraging, even if a significant oscillation of the shock wave has not been observed. The presence of a multiple shock-waves pattern and some coherent structures have been observed. Temporal spectra have been realized upstream of the shock-wave boundary layer interaction, near the lower wall, to better characterize by means of frequencies, the phenomenon visualized.

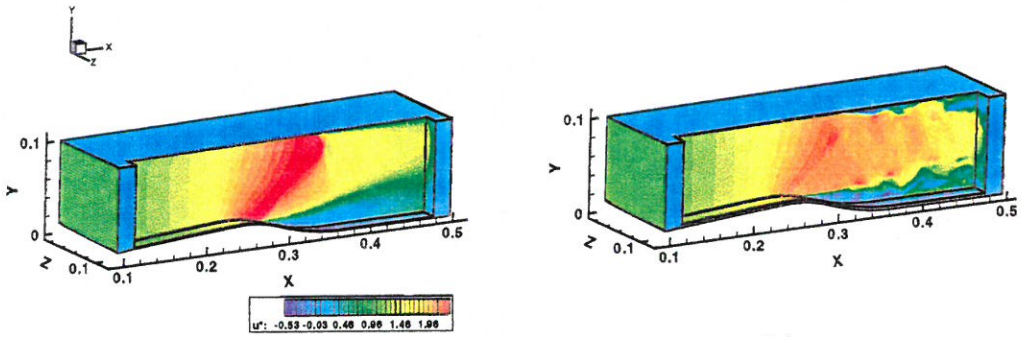

(a) (b)

FIG. 3 – *(a) Initial RANS field* $\langle u \rangle$ *- (b) Unsteady LES field* $\tilde{u}$

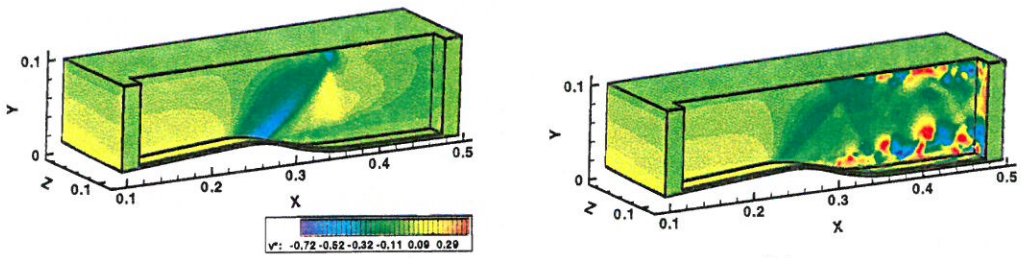

(a) (b)

FIG. 4 – *(a) Initial RANS field* $\langle v \rangle$ *- (b) Unsteady LES field* $\tilde{v}$

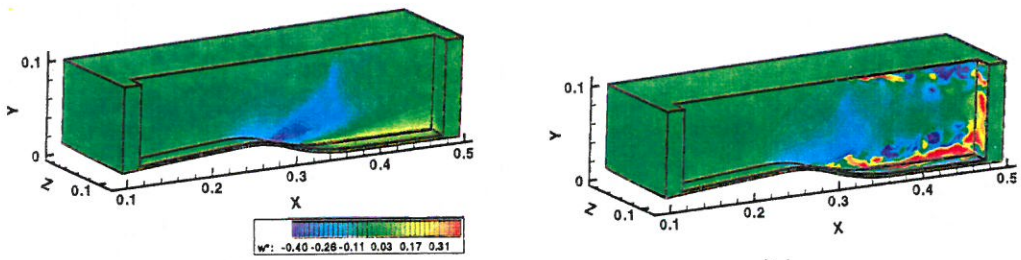

(a) (b)

FIG. 5 – *(a) Initial RANS field* $\langle w \rangle$ *- (b) Unsteady LES field* $\tilde{w}$

We now present the temporal spectrum of the spanwise fluctuations of the velocity, $w' = \widetilde{w} - \langle \widetilde{w} \rangle$, at $x = 0.498$ m, near the lower wall. The analysis of the spanwise fluctuations in time has been preferred to the longitudinal ones because the mean flow $\langle \widetilde{w} \rangle$ is much smaller than $\langle \widetilde{u} \rangle$ so the unsteady pertubations are better captured. Both transverse velocity components, $\widetilde{v}$ and $\widetilde{w}$, are well adapted variables to characterize the larges coherent structures in shear layers [19]. The fluctuations w' have been selected, instead of v', because $\widetilde{w}$ is the component that injects some fluid in the dead water but they behave in a very similar way.

The spectrum of w' has been plotted for ten points along (Oz) in figure (9a), from the left side wall to the right side wall. The different locations are figured out in the sketch of the channel figure (8). For each z location, the energy of the spanwise fluctuations is plotted versus the Strouhal number. The Strouhal number corresponds to a dimensionless frequency defined as : $St = \dfrac{f\ yb}{u_{ref}}$. The length yb is the maximum height of the bump with $yb = 0.02$ m. It can be observed, in figure (9a), that the most energetic low frequencies are located near the wall where the intensity of the shock-wave/boundary layer interaction is strong enough to observe the 3D recirculation (see figure (6b)) and where the rollups appear [32].

The w' fluctuations spectrum at $z = 0.119$ m, near the right lateral wall, is then presented in more detail, in figure (9b). The spectrum, in figure (9b), presents three distinguished parts characterized by a different slope. In the low Strouhal numbers part of the spectrum, one can observe that large energetic scales are produced at a Strouhal number close to $St \simeq 0.4$. This value is in agreement with the bluff body Strouhal number of 0.3 measured in the wake. This result is also coherent with the ones presented by L. M. Hudy and al. in [32], even if our value is higher. This can be explained by the fact that our simulation is 3D while their results are 2D. Turbulence is then more developed in the present simulation. At $St \simeq 1.3$ the spectrum slope changes and the energy intensity decreases rapidly with St. This energy diminution is associated with the dissipation induced by the model and the numerical scheme. The unsteady phenomena characterized by the frequencies between $St \simeq 1.3$ and $St \simeq 7$ are more sensitive to the numerical and physical dissipation than the large scales. The third region of the spectrum, from $St \simeq 7$, is not significant and corresponds to extra resolution.

Under a Taylor's scale hypothesis validity, one can write that $f = \widetilde{u}_{local}\ k$, where k is the wave number of the phenomena. The usual curves $St^{-5/3} \equiv k^{-5/3}$ and $St^{-4} \equiv k^{-4}$ have then been plotted in figure (9b) [38]. The $St^{-5/3}$ curve's slope agrees very well with the spectrum's mean slope in the low Strouhal numbers range. This is also the case with the St^{-4} curve's slope in the dissipative range. The spatial scale corresponding to the Strouhal number St is calculated by $l_c = \dfrac{u_{loc}\ y_b}{St\ u_{ref}}$. Following the results obtained in [14], $u_{loc} \simeq \dfrac{u_{ref}}{4}$ at this location. Then the scale associated to the first change in the slope of the spectrum, around $St \simeq 1.3$, is of order of $l_c = 4\ 10^{-3}$ m. This length is connected to the dissipative scale induced by the numerics, and is of the order of the longitudinal grid mesh size value (at this location, $\Delta x >> \Delta y \simeq \Delta z$). This result agrees with the

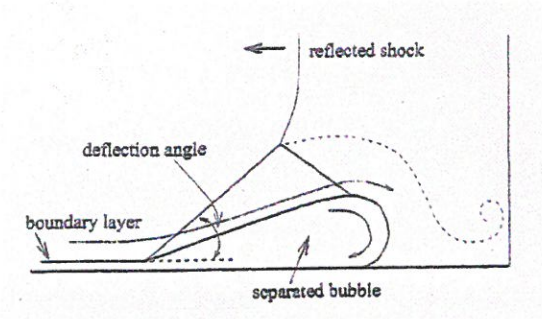

Figure 7: Bifurcated shock pattern

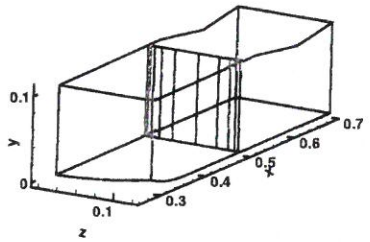

Figure 8: w' spectrum locations along (Oz)

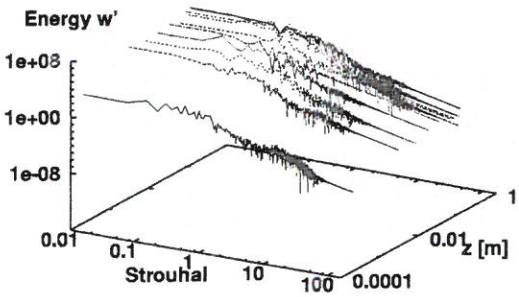

(a)

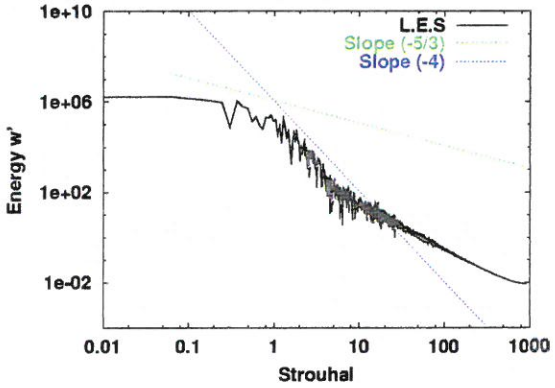

(b)

Figure 9: w' : (a) Spectra against the St number and along (Oz) - (b) Spectrum against the St number at $z = 0.119$ m

framework of LES, where only the energetic structures, convected by u_{loc} and that are larger than the grid mesh size, are directly solved.

5.3 Results on the mean value of the velocity components and of the Reynolds stress tensor : comparison with RANS and experiments

We now present the time average results obtained on the velocity and the Reynold stress tensor components. The LES results are compared to both the experiments [6], and the RANS results obtained by using the Launder-Shima model [27].

We recall that the volume explored by the experiments is included between $x = 0.230$ m and $x = 0.390$ m (see figure 2). Experimentally, $x = 0.230$ m crosses the bump upstream of the shock-wave/boundary layer interaction. The planes $x = 0.270$ m and $x = 0.290$ m are still on the bump, at the beginning of the shock wave/boundary layer interaction. The planes cut the foot of the shock wave near the lower wall. Both planes $x = 0.310$ m and $x = 0.340$ m coincide with the dead water region close to the lower wall. $x = 0.360$ m

cuts the shock wave near the upper wall. Then $x = 0.390$ m is far downstream of the interaction, but still in a region where the boundary layer slightly relaxes to its unperturbed state. Only the differences observed in the planes (y, z) where the boundary layer separates will be discussed in the paper, as the aim of this study is to analyze the 3D shock-wave boundary layer interaction and its LES modelization.

The profile along (Oy) of the mean values of the velocity and Reynolds stress components are then compared to the components measured experimentally and simulated with RANS. A good agreement between RANS and LES is observed upstream of the interaction. The comparison between the present results with experiments and RANS is difficult within the 3D shock wave/boundary layer interaction. It can be observed in the snapshots of the unsteady flow fields, in figures (4b), (5b) and (6b), that the RANS location of the shock wave in the channel, in good agreement with the experimental one, is not well recovered in our simulation. This was also observed in the previous simulation performed with a second order TVD scheme in [13]. The location of the interaction in the LES is slightly upstream of the experimental and RANS one. To compare more precisely our results with the experimental and statistical ones, the different profiles under analysis have been plotted for identical fictive abscissa $(x_{expe} - x_{shock})$.

Before presenting these results, we discuss in detail the probable origins of the wrong location of the shock-wave in the channel predicted by the LES.

5.3.1 Location of the shock-wave/boundary layer interaction in the channel

Figure (10) presents the mean velocity profile of the three velocity components $\langle\widetilde{u}\rangle$, $\langle\widetilde{v}\rangle$ and $\langle\widetilde{w}\rangle$ at $x = 0.230$ m and $z = 0.1113$ m. This location is upstream of the shock wave/boundary layer interaction. The LES results, plotted in red, are in good agreement with the initial RANS fields, plotted in blue. The main differences between the curves, at this location, come from the up and down boundary layers that are thinner in the LES. Yet, it can be observed that the longitudinal velocity component, $\langle\widetilde{u}\rangle$, is overestimated by RANS, and so by LES. We can underline that this is the case all along the spanwise direction. This might come from a too important thickeness of the boundary layers at the initialization in the RANS simulation [27]. The over flow rate observed in figure (10) then balances the boundary layers thickening. The opening of the throat in the RANS simulation has been adapted to recover the location of the shock wave in the channel corresponding the statistical modeling flow conditions in the channel. At this location, $y_{RANS}^{secondthroat} = 0.095$ m instead of $y_{EXPE}^{secondthroat} = 0.0956$ m [27].

The channel's geometry used in the simulation is the same as in the RANS one. Also, the initial RANS inlet flow rate is prescribed as the LES is initialized with the statistical converged field that was obtained by using the Launder-Shima model. It seems that the upstream location of the shock wave in the divergent in the LES can be explained by the different flow field obtained by the LES in the entire channel, unadapted to the RANS geometry and flow rate. An inviscid analysis permits to better understand the physical phenomenon. In such kind of analysis the flow is considered as a longitudinal succession of cross sections, uniform in the tranverse directions. The flow rate, $\dot{m} = \int_A \rho \overrightarrow{u}.\overrightarrow{dS}$ is then given by $\dot{m} = \psi(\gamma)\frac{A_2\ \gamma\ Pt_2}{c_2}$ through the second throat [21]. This flow rate is fixed as the

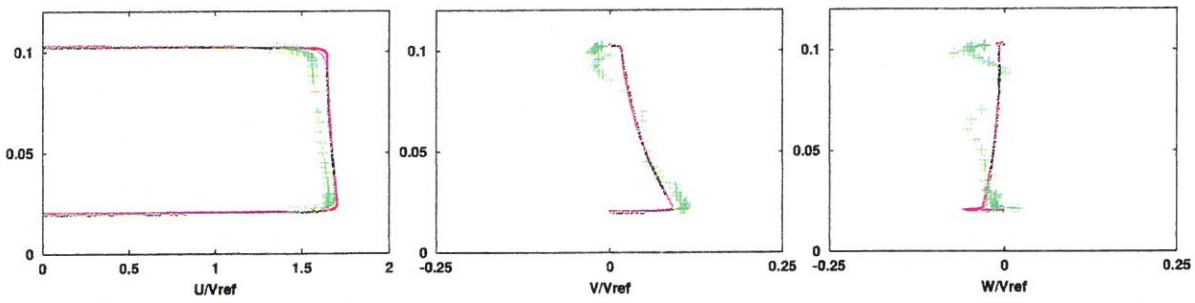

Figure 10: $\langle\widetilde{u}\rangle/u_{ref}$, $\langle\widetilde{v}\rangle/u_{ref}$, $\langle\widetilde{w}\rangle/u_{ref}$ at $x = 0.230$ m and $z = 0.1113$ m : WENO : - ; RANS : - ; EXPE : +++

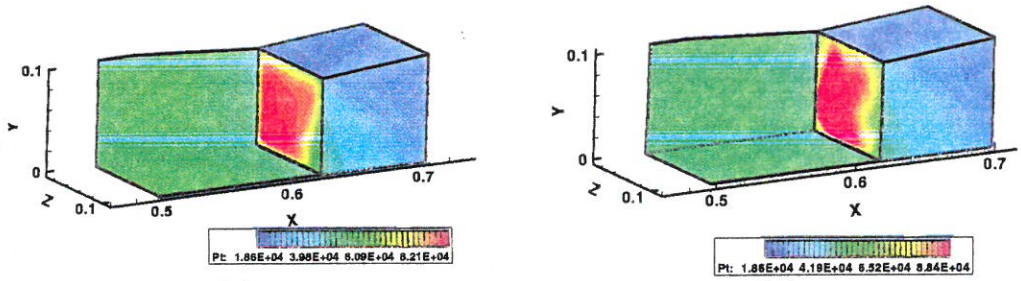

(a) (b)

Figure 11: (a) Initial RANS field $\langle Pt\rangle$ - (b) LES field $\langle\widetilde{Pt}\rangle$

flow is in a choking state and is the same as in the first sonic throat, $\dot{m} = A_2\ Pt_2 = A_1\ Pt_1$ with $Pt_1 = Pt = 0.92\ 10^5$ Pa the inlet total pressure. The variable A_k represents the area of the k-th section, while c_k represents the sound celerity and Pt_k the total pressure in the k-th section. The ratio $\dfrac{Pt_2}{Pt_1}$ corresponds to the loss of the total pressure through the shock wave. It is the control parameter of the shock wave location in the channel, when the geometry is given. The total pressure at the initial state and the total pressure predicted by LES have then been plotted figures (11a) and (11b) in the second throat. It can be observed that $\dfrac{Pt_{2LESmax}}{Pt_1} = 0.961$ instead of $\dfrac{Pt_{2RANSmax}}{Pt_1} = 0.892$. The high value of Pt_2 in the LES ensures the flow rate conservation as the cross section of the second throat is underestimated and the flow rate overestimated since the initialization. The ratio $\dfrac{Pt_2}{Pt_1}$ evolution through a shock-wave is a decreasing function of the mach number, so the Mach number upstream of the shock-wave is lower than in the RANS simulation explaining the upper location of the shock-wave [21].

5.3.2 Results on the mean value of the velocity component

The profiles are plotted for identical fictive abscissa $(x_{expe} - x_{shock})$ and versus a dimensionless vertical length $y^* = (y - y_{bump})/(y_{max} - y_{bump})$. The coordinate x_{shock} has been calculated by using the results obtained on the Isentropic Mach number on the

lower wall, at $z = 0.106$ m. The figure (12) represents the Isentropic Mach number, $M_{is} = \sqrt{(\frac{2}{\gamma - 1}[(\frac{P_t}{\langle \overline{p} \rangle})^{\frac{\gamma-1}{\gamma}} - 1])}$, along (Ox), at this location. It can be observed that the experiments and the numerical results agree very well upstream of the 3D interaction. The intensity of the shock wave predicted by LES is smaller than the experimental and RANS one. It can nevertheless be observed that the experimental pronounced pressure plateau in the stagnation zone below the legs of the shock, which is characteristic of a shock/boundary layer interaction, is predicted by LES, on the opposite of RANS.

The experimental coordinate of the shock wave has been evaluated by $x_{shock} = 0.26$ m and the coordinate calculated by LES by $x_{shock} = 0.2476$ m.

Figure (13) presents the mean velocity profile of the three velocity components $\langle \widetilde{u} \rangle$, $\langle \widetilde{v} \rangle$ and $\langle \widetilde{w} \rangle$ at $(x_{expe} - x_{shock}) = 0.03$ m and $z = 0.0913$ m. This plane crosses the bump close to the lower wall. The shock wave clearly appears in the experimental velocity profiles. The foot of the oblique shock and the plane $(xexpe - x_{shock}) = 0.03$ m intersection is located near the lower wall. The three measured velocity components present a discontinuity around $y^* = 0.02$. RANS does not yet predicts the presence of the shock-wave, because its location is a little upstream of the experimental one. LES predicts a location of the shock around $(y - y_{bump})/(y_{max} - y_{bump}) = 0.025$. The boundary layer is already separated in the LES, and then thicker than in the RANS simulation and experiments. Experimentally, the flow is accelerated on the bump. As the bump is asymmetric, it is deviated towards the far lateral wall. This is visualized by the negative vertical and spanwise experimental and statistical components in figure (13). The vertical velocity component intensity predicted by LES is smaller than the experimental one, because of the large thickening of the boundary layer. The shape of the curve stays anyhow close to experiments. The positive value near the lower wall in the LES can be explained by the fact that the flow has to cross the small recirculation visible on the longitudinal velocity component. Finally, it can be observed that the double peaks measured experimentally on the spanwise component are predicted by LES even if they are located closer to the lower wall than in experiments.

Figure (14) represents the mean velocity profile of the three velocity components $\langle \widetilde{u} \rangle$, $\langle \widetilde{v} \rangle$ and $\langle \widetilde{w} \rangle$ at $(x_{expe} - x_{shock}) = 0.13$ m and $z = 0.1113$ m where the experimental lower boundary layer is no longer separated. It can be underlined that both simulations predict a separation near the upper wall, which is not recovered experimentally. In the lower part of the channel, that the LES predicts a less important thickening than experiments and RANS. This probably results from the upstream shock-wave/boundary layer interaction and the less important shock wave's intensity in the simulation. It can be also explained by the multiple shock-wave pattern observed in the unsteady results. The negative value of the longitudinal velocity component in the LES, very close to the lower wall, characterizes the structures already observed in the spectrum of w' at low frequencies. The RANS simulation presents a good agreement with experiments in the upper channel's part. Nevertheless, it overpredicts the recirculation zone, near the lower wall, as the longitudinal velocity component is negative in the entire boundary layer. It can be observed that the longitudinal velocity component calculated by LES becomes positive

before the one calculated by RANS. Experimentally, after the end of the bump, the flow is reinjected in the recirculation limiting the longitudinal extent of the bulbe and leading to the 3D properties of the interaction. Then the experimental vertical component is negative and the experimental spanwise component is positive and quite strong close to the lower wall. The vertical velocity profile is neither well recovered by RANS nor LES. The strong vertical injection calculated with the LES near the lower wall compensates the longitudinal velocity deficit observed near the lower wall at this location. The transverse velocity profile $\langle \widetilde{w} \rangle$ simulated by LES, is different from experiments very very close to the lower wall, and also near the upper wall, but the LES recovers the strong injection of transverse fluid around $y^* = 0.01$. This is an important modeling feature as this strong injection contributes to limit the recirculation zone extent in the longitudinal direction. At this location, LES predicts a negative value of $\langle \widetilde{w} \rangle$ very close to the lower wall before becoming positive, which is probably correlated to the unsteady longitudinal structures predicted by LES in figure (6b).

Finally, the figures (15) and (16) represent the skin friction line patterns obtained on the lower wall by experiments and RANS figure (15), and by LES in figure (16). It allows a better identification and comparison of the main separation and attachment line between LES, RANS and experiments. The patterns have been centered around the recirculation zone, just downstream of the bump. The experimental focus F_1 observed in the figure (15), around which rolls up the separation line and the skin friction lines coming from upstream, is also well visible in the RANS and LES results. Its location along the spanwise direction is better predicted by LES than by RANS. The RANS location prediction is above from the experimental one. Experimentally, it is located at $z = 0.40$ m which correspond to the prediction $z = 0.80$ m in the LES, as the coordinates system is reverse. The point C_2 is the intersection of the attachment line with the wall measured experimentally. It is located around $x = 0.4$ m. This point does not appear in the RANS skin friction patterns but it is located almost at $x = 0.44$ m in the LES, which is slightly downstream of the experiments but upstream of the RANS location. This results underline again the interesting feature of the LES modeling which allows to better recover the experimental longitudinal extent of the dead water zone. It can also be observed that the LES and RANS simulation predict a small recirculation near the upper wall, around $x = 0.45$ m for LES, that is not measured experimentally.

5.3.3 Results on Reynolds stress tensor components

We now discuss the prediction of the LES on the Reynolds stress tensor components. In connection with the velocity profiles presented in the previous subsection, the profiles of the six components of the Reynolds stress tensor versus (Oy), are plotted at $(x_{expe} - x_{shock}) = 0.03$ m, $z = 0.0913$ m. Then, to study in detail the turbulence properties of the flow and its LES modelization within the interaction zone, the six components of the Reynolds stress tensor are also presented at $(x_{expe} - x_{shock}) = 0.08$ m, $z = 0.1113$ m. All the curves are plotted versus $y^* = (y - y_{bump})/(y_{max} - y_{bump})$.

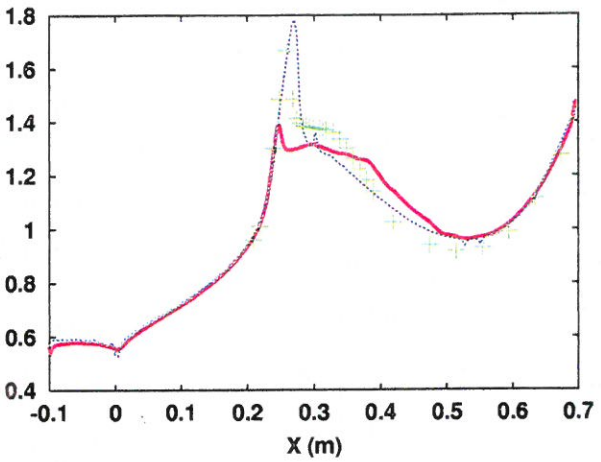

Figure 12: Isentropic Mach number along (Ox) at $z = 0.106$ m on the lower wall: WENO : - ; RANS : - ; EXPE : +++

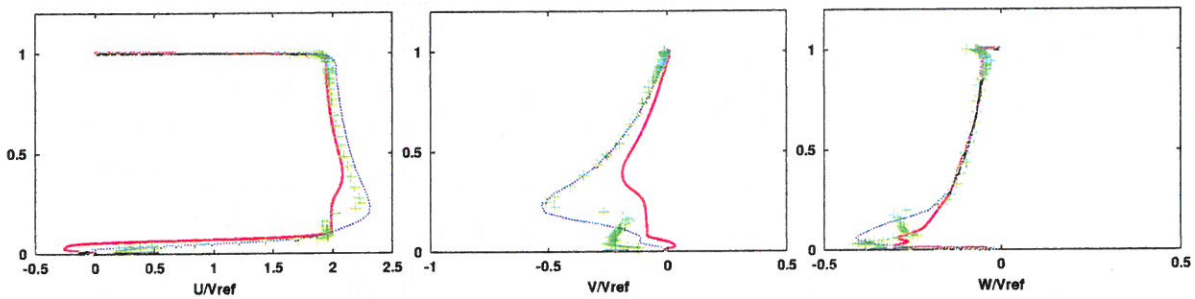

Figure 13: $\langle\widetilde{u}\rangle/u_{ref}$, $\langle\widetilde{v}\rangle/u_{ref}$, $\langle\widetilde{w}\rangle/u_{ref}$ for $\Delta x = 0.03$ m and $z = 0.0913$ m : WENO : - ; RANS : - ; EXPE : +++

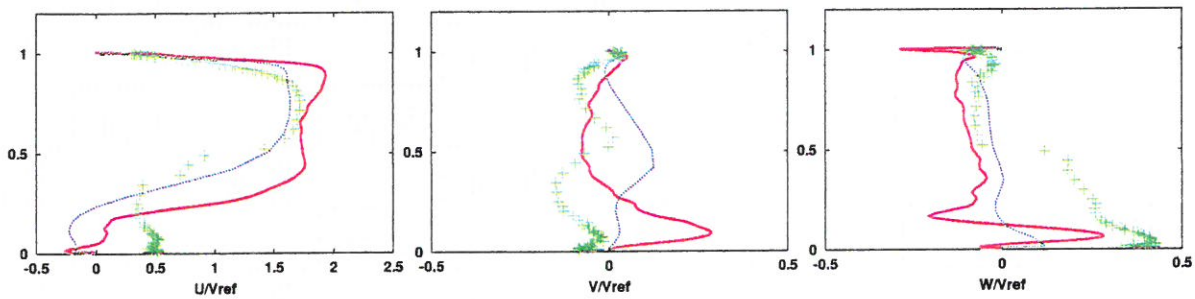

Figure 14: $\langle\widetilde{u}\rangle/u_{ref}$, $\langle\widetilde{v}\rangle/u_{ref}$, $\langle\widetilde{w}\rangle/u_{ref}$ at $\Delta x = 0.13$ m and $z = 0.1113$ m : WENO : - ; RANS : - ; EXPE : +++

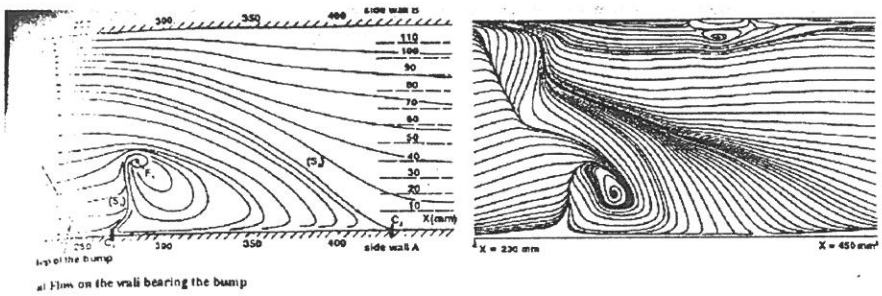

Figure 15: Experimental and $k - \varepsilon$ skin friction line patterns [6]

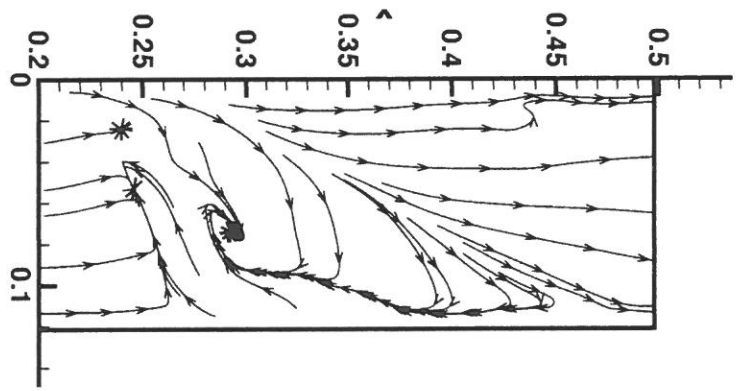

Figure 16: LES skin friction line patterns

The measured intensity of $\widehat{u'''u'''}$ in the shock foot, in figure (17), presents an important turbulent peak near the lower wall. If one considers the production term of the $\widehat{u'''u'''}$ transport equation, written for simplicity for an incompressible flow [18] :

$$P = -2\ \widehat{u'''v'''}\frac{\partial \widetilde{u}}{\partial y} - 2\ \widehat{u'''u'''}\frac{\partial \widetilde{u}}{\partial x}$$

the presence of the peak can be explained by the high positive value of the two different terms. The experimental shear stress $\widehat{u'''v'''}$ at this location, in figure (18), is negative and important, leading to a high positive value of the first term of P. The streamwise derivative of $\widetilde{u}$ is as large as the term involving $\dfrac{\partial \widetilde{u}}{\partial y}$ because of the retardation of the whole dissipative flow [18]. The turbulent peak intensity of $\widehat{u'''u'''}$ is overpredicted by LES. On the other hand, LES predicts a very low turbulent intensity on $\widehat{v'''v'''}$ and $\widehat{w'''w'''}$ profiles in the boundary layer, in figure (17). Following the description in [18], the production of the transverse components $\widehat{v'''v'''}$ and $\widehat{w'''w'''}$ decreases in the first part of the interaction. The reason of the strong intensity turbulence on $\widehat{u'''u'''}$ might then be the bad distribution of the total kinetic energy between the three components $\widehat{u'''v'''}$, $\widehat{v'''v'''}$ and $\widehat{w'''w'''}$. Let us underline, anyway, that the turbulent intensity level of $\widehat{w'''w'''}$ is neither well recovered by RANS. It can be observed on the correlations $\widehat{v'''v'''}$ and $\widehat{u'''v'''}$ that the turbulent peak measured experimentally around $y^* = 0.02$ is predicted by LES. This peak corresponds to the shock-wave fluctuations. Its location is shifted from the experimental one probably because of the upstream location of the shock wave. Let us recall that the abscissa coordinate of the shock wave has been evaluated on the lower wall, and that this location varies along (Oy). The transverse correlations $\widehat{u'''w'''}$ and $\widehat{v'''w'''}$ are also plotted in figure (18). It can be observed that neither RANS nor LES recover the turbulent intensity near the lower wall.

Figures (19) and (20) present the six Reynolds stress tensor components at $(x_{expe} - x_{shock}) = 0.08$ m and $z = 0.1113$ m. Experimentally, as it was observed in the velocity profiles, the boundary layer that is thicker than in the upstream region is relaxing towards its equilibrium state after its the shock wave/boundary layer interaction. The longitudinal correlations $\widehat{u'''u'''}$ presents a peak of turbulent intensity, in the lower part of the channel, coming from the high turbulent shear stress $\widehat{u'''v'''}$ observed in figure (20). The turbulent shear stress is important at this location because of the shock wave/boundary layer interaction. LES and RANS predict a higher turbulent $\widehat{u'''u'''}$ intensity than experiments because the boundary layer is thicker as it is still separated in both simulations (see figure 13), on the opposite of the experiments. The redistribution on the normal component $\widehat{w'''w'''}$ is not well recovered by RANS and LES even if $\widehat{v'''v'''}$ and $\widehat{w'''w'''}$ are better predicted by LES at this location than at $(x_{expe} - x_{shock}) = 0.03$ m. The production of these transverse components increase in this part of the interaction [18] making the redistribution term less predominant in the turbulent kinetic equation. This may explain that the LES peak is not as over estimated as in figure (17). Still in figure (19), in the longitudinal correlation profile, it can be observed that LES predicts a strong turbulent peak intensity near the upper wall. This must be linked to the pesence of the shock-wave coupled with a separation zone predicted by LES all along the spanwise direction in the foot of the upper shock (see figure (13)). To end with, the correlations

$\widehat{u'''w'''}$ and $\widehat{v'''w'''}$ are plotted in figure (20). The measured profile show a large scattering in the data near the lower wall. The peak near the upper wall observed on $\widehat{u'''w'''}$ profile predicted by LES comes from the separated boundary layer prediction. Again, it can be observed that neither RANS nor LES recover the experimental data.

Following P. Moin and J. Kim in [42], it seems that the other reason which can explain the systematic over prediction of the turbulent intensity is the grid resolution in the longitudinal direction Ox.

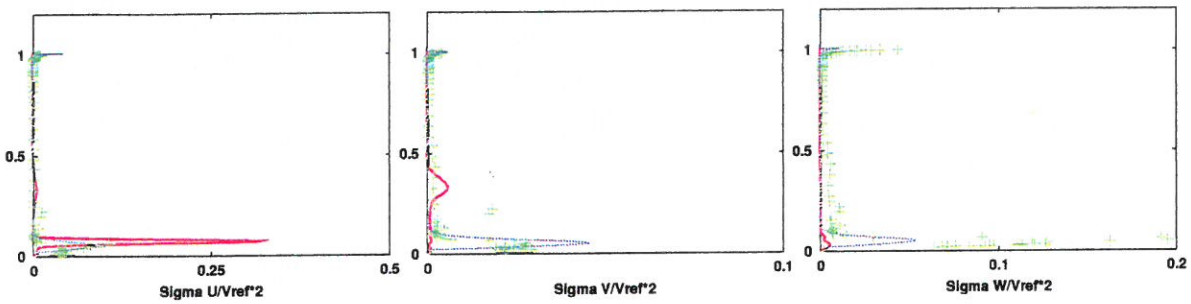

Figure 17: $\widehat{u'''u'''}/u_{ref}^2$, $\widehat{v'''v'''}/u_{ref}^2$, $\widehat{w'''w'''}/u_{ref}^2$ at $\Delta x = 0.03$ m and $z = 0.0913$ m : WENO : - ; RANS : - ; EXPE : +++

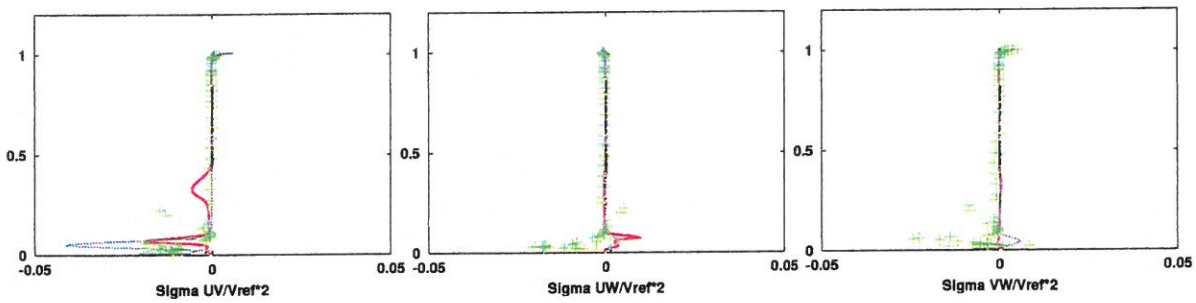

Figure 18: $\widehat{u'''v'''}/u_{ref}^2$, $\widehat{u'''w'''}/u_{ref}^2$, $\widehat{v'''w'''}/u_{ref}^2$ at $\Delta x = 0.03$ m and $z = 0.0913$ m : WENO : - ; RANS : - ; EXPE : +++

6 Conclusions and outlooks

The simulation of a compressible turbulent flow through a 3D transsonic channel has been performed by using LES, in sight of turbomachinery applications. The flow simulated presents the main charateristics of the flows encountered in turbomachinery. A 3D shock-wave/boundary layer interaction is located downstream of the bump, characteristic phenomenon encountered in turbines or compressors in unadapted conditions. Also, the test case presents available experiments (ONERA, Delery) and RANS simulations (LEMFI) performed with the Launder-Shima $R_{ij} - \varepsilon$ turbulence modeling.

The computational configuration and the inflow characteristics have been first described. Then the compressible spatially filtered Navier-Stokes equations have been specified with the two preserved subgrid terms. The subgrid stress tensor has been modeled by

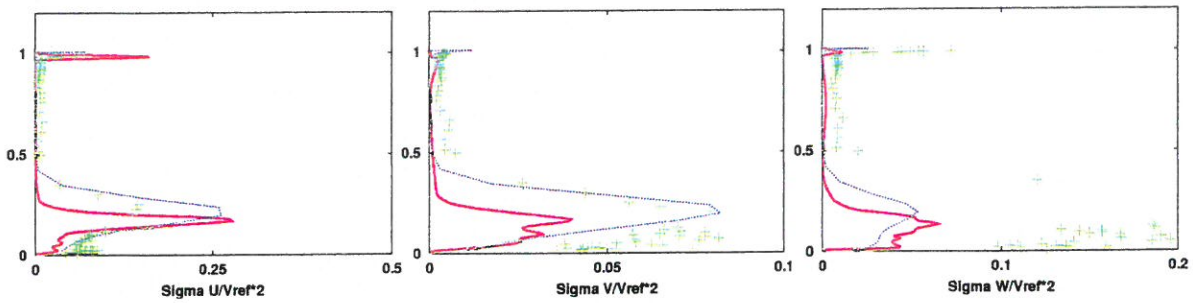

Figure 19: $\widehat{u'''u'''}/u_{ref}^2$, $\widehat{v'''v'''}/u_{ref}^2$, $\widehat{w'''w'''}/u_{ref}^2$ at $\Delta x = 0.08$ m and $z = 0.1113$ m : WENO : - ; RANS : - ; EXPE : +++

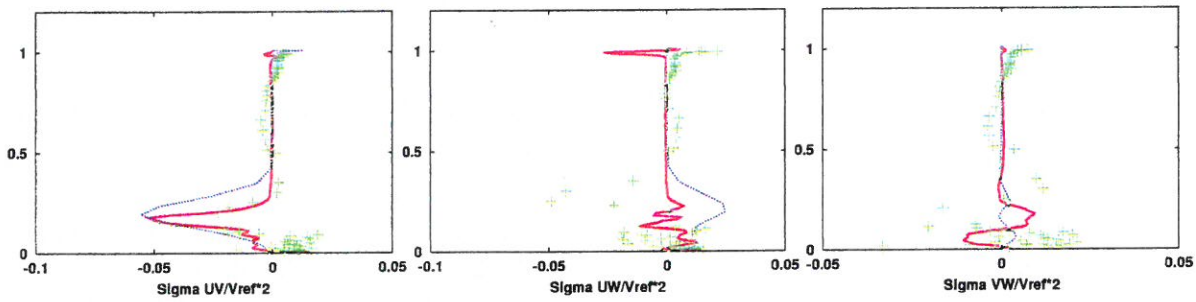

Figure 20: $\widehat{u'''v'''}/u_{ref}^2$, $\widehat{u'''w'''}/u_{ref}^2$, $\widehat{v'''w'''}/u_{ref}^2$ at $\Delta x = 0.08$ m and $z = 0.1113$ m : WENO : - ; RANS : - ; EXPE : +++

using the mixed scale model through a Boussinesq hypothesis. The subgrid heat flux has been evaluated by a first gradient hypothesis through a constant Prandtl number assumption. The LES equations have been integrated in time by using an explicit third order R-K scheme and the spatial discretization of the convective terms has been performed with a thrid order WENO shock capturing scheme. Then the boundary conditions and the initialization have been described in detail, before analyzing the different results obtained in the channel by the LES.

The unsteady results have shown that the LES fields are very different from the initial steady state. They are very interesting in sight of turbomachinery applications. The spectrum of the spanwise fluctuations, performed in the recirculation, has permitted to capture the low characteristic frequency corresponding to the ejection of the large unsteady structures. Spatial correlations have also been recorded to better characterize the coherent structures. It has permitted to conclude that the corresponding turn over time of the large scales is significantly smaller than the simulation time, so we can suppose that we have correctly captured the dynamics of the large scales structures with the simulation.

The results on the mean velocity components obtained by LES show that the simulation predicts an upstream location of the shock wave in the channel, with an intensity smaller than the experimental one. Anyway, with an appropriated scaling of the curves along (Ox), the results are coherent with experiments. The main result of their analysis is the good prediction by LES of the strong injection of fluid in the streamwise direction. It limits the longitudinal extent of the recirculation as measured experimentally. The

prediction of LES on the Reynolds stress tensor components are in good agreement with experiments within the recirculation zone. Yet, the strong anisotropy exhibited by the flow is not well recovered, neither by RANS nor LES modeling.

The LES simulation of this 3D compressible unsteady, turbulent, complex flow has shown the strong potentialities of the methodology in the prediction of industrial unsteady complex flows. It should be then interesting to pursue the study by testing the influence of the opening of the second throat on the LES results. The section area of the second throat used here was linked to the flow field obtained by RANS. As we have prescribed the RANS conditions inflow, we would like to test the inlet flow rate change effects on the LES when using the experimental area section value of the second throat. Also, special attention will have to be paid to the anisotropic behaviour of the subgrid models.

We can underline, to end with, that an adaptative grid method should be tested in the future on this complex 3D case to reduce the computational cost that is still very important at present.

Acknowlegments : Thanks go to CIRT (SNECMA, EDF, ABB-Alstom), to the LEMFI and to IDRIS.
Many thanks also to G. A. Gerolymos, I. Vallet (LEMFI) and J. Delery (ONERA) for our numerous discussions and their valuable comments.

References

[1] N. A. Adams. Direct simulation of the turbulent boundary layer along a compression ramp at $M = 3$ and $Re_\theta = 1685$. *J. Fluid Mech*, 420:47–83, 2000.

[2] B. S. Balwin and H. Lomax. Thin layer approximation and algebraic model for separated turbulent flows. In *AIAA Paper no 78-257, 16th ASM, Huntsville, Alabama*, 1978.

[3] J. Bardina, J. H. Ferziger, and W. C. Reynolds. Improved subgrid scale models for large eddy simulation. In *AIAA 13th, Fluid & Plasma Dynamics Conference*, 1980.

[4] T. J. Barth and H. Deconinck. *High-Order Methods for Computational Physics.* Springer, 1999.

[5] C. Brun and R. Friedrich. A-priori tests of SGS stress models in fully developed pipe flow and a new local formulation. In Kluwer Academic Publishers, editor, *Ercofact Series, Direct and Large-Eddy Simulation III*, 1999.

[6] J. Cahen, V. Couaillier, J. Délery, and T. Pot. Validation of code using turbulence model applied to three-dimensional transonic channel. *AIAA Journal*, 33(4), 1995.

[7] L. Cambier and B. Escande. Calculation of a three-dimensional shock wave-turbulent boundary-layer interaction. *AIAA Journal*, 28(11):1901–1908, 1990.

[8] B. F. Carroll and J. C. Dutton. Turbulence phenomena in a multiple normal shock wave/turbulence boundary-layer interaction. *AIAA Journal*, 30:43–48, 1992.

[9] V. Carstens and S. Schmitt. Investigation of fluid-structure interaction in vibrating cascades using a time domain method. In *ISUAAAT'2000 and First Legendre Lecture Series*, Lyon, 2000.

[10] J. C. Chassaing and G. A. Gerolymos. Compressor flutter analysis using time-nonlinear and time-linearized 3D Navier-Stokes methodes. In *ISUAAAT'2000 and First Legendre Lecture Series*, Lyon, 2000.

[11] P. Comte and M. Lesieur. Large-eddy simulations of compressible turbulent flows. In *Lecture Series 1998-05, Advances in Turbulence Modelling*, 1998.

[12] L. Coquart. Numerical simulation of the flow through an over-expanded thrust-optimized nozzle, investigated experimentally in the r2ch blowdown wind tunnel at onera. Technical report, LIMSI-CNRS, 2003-08, 2003.

[13] L. Coquart, C. Tenaud, and L. Ta Phuoc. LES of a turbulent compressible flow in a 3D channel : comparison with RANS and experiments. In *Proceedings of the Euromech Colloquium 403*, Poitiers-Futuroscope, France, 1999. J. P. Bonnet and S. Barre.

[14] L. Coquart, C. Tenaud, and L. Ta Phuoc. LES of a three dimensional shock-wave/boundary layer interaction in a channel flow. In *Proceedings of the ASME Fluids Engineering Division Summer Meeting*, Montreal-Canada, 2002. ASME.

[15] T. J. Craft. Developments in a low-reynolds-number second-moment closure and its application to separating and reattaching flows. *International Journal of Heat and Fluid Flow*, 19:541–548, 1998.

[16] M. R. Visbal D. P. Rizzeta and D. V. Gaitonde. Large eddy simulation of supersonic compression-ramp flow by high order method. *AIAA Journal*, 39:2283–2292, 2001.

[17] V. Daru, G. Fernandez, and C. Tenaud. On CFD to investigate bifurcated shock wave pattern. In Great Keppel Island, editor, *Issw21*, Australia, 1997.

[18] J. M. Délery. Experimental investigation of turbulence properties in transonic shock/boundary-layer interactions. *AIAA Journal*, 21(2):180–185, 1983.

[19] L. Doris, C. Tenaud, and L. Ta Phuoc. LES of spatially developing 3d compressible mixing layer. *C. R. Acad. Sci. Paris*, 328, Serie II b:567–573, 2000.

[20] F. Ducros, P. Comte, and M. Lesieur. Large-eddy simulation of transition to turbulence in a boundary layer developing spatially over a flat plate. *J. Fluid Mech*, 326:1–36, 1996.

[21] H. W. Liepmann et A. Roshko. *Eléments de la dynamique des gaz.* Gauthier-Villars et Cie Editeur Paris, 1962.

[22] A. Favre. Equations des gaz turbulents compressibles ; ii.- méthode des vitesses moyennes, méthode des vitesses macroscopiques pondérées par la masse volumique. *Journal de Mécanique*, 4, 1965.

[23] C. Ferreira Gago, S. Brunet, and F. Garnier. Numerical investigation of turbulent mixing in a jet wake vortex interaction. *AIAA Journal*, 10(2):276–284, 2002.

[24] C. Ferreira Gago, F. Garnier, and F. Utheza. Large eddy simulation of a hot round jet : assessment of subgrid scale modeling. In *Advances in Turbulence, Proceedings of the Ninth European Turbulence Conference, Southampton UK*, 2002.

[25] E. Garnier and al. On the use of shock-capturing schemes for large eddy simulation. *Journal of Computational Physics*, 153:273–311, 1999.

[26] M. Germano, U. Piomelli, P. Moin, and W. H. Cabot. A dynamic subgrid-scale eddy-viscosity model. *Phys. Fluids A.*, 3:1760–1765, 1991.

[27] G. A. Gerolymos and I. Vallet. Near-wall reynolds-stress three-dimensional transonic flow computation. *AIAA Journal*, 35(2):228–236, 1997.

[28] G. A. Gerolymos and I. Vallet. Wall normal free near-wall reynolds-stress closure for 3D compressible separated flows. *AIAA Journal*, 1999.

[29] G. A. Gerolymos and I. Vallet. Wall normal free reynolds-stress model for compressible rotating flows applied to turbomachinery. *AIAA Journal*, 2000.

[30] K. Hanjalić. Advanced turbulence closure models : a view of current status and future prospects. *International Journal of Heat and Fluid Flow*, 15(3):178–203, 1994.

[31] Klaus A. Hoffmann. *Computational Fluid Dynamics for Engineers.* Engineering Education System, 1989.

[32] L. M. Hudy, A. M. Naguib, W. M. Humphreys, and Scott M. Bartram. Wall-pressure-array measurements beneath a separating / reattaching flow region. In *40th Aerospace Sciences Meeting and Exhibit, AIAA 2002-0579, Reno*, 2002.

[33] G.-S. Jiang and C.-W. Shu. Efficient implementation of weighted ENO schemes. *Journal of Computational Physics*, 126:202–228, 1996.

[34] J. Jiménez. On Eddy-viscosity sub-grid models. In Kluwer Academic Publishers, editor, *Ercofact Series, Direct and Large-Eddy Simulation III*, 1999.

[35] E. Lenormand, P. Sagaut, L. Ta Phuoc, and P. Comte. Subgrid-scale models for large-eddy simulations of compressible wall bounded flows. *AIAA Journal*, 38(8):1340–1350, 2000.

[36] M. A Leschziner, P. Batten, and H. Loyau. Modelling shock-affected near-wall flows with anisotropy-resolving turbulence closures. *International Journal of Heat and Fluid Flow*, 21:239–251, 2000.

[37] M. A Leschziner, H. Loyau, and D. Apsley. Prediction of shock/boundary-layer interaction with non-linear eddy-viscosity models. In *ECCOMAS 2000, Barcelona*, 2000.

[38] M. Lesieur. *Turbulence in fluids.* Kluwer Academic Publishers, 1990.

[39] M. Lesieur and P. Comte. Favre filtering and macro-temperature in large eddy simulations of compressible turbulence. *C. R. Acad. Sci. Paris*, 329, Serie II b:363–368, 2001.

[40] X. Liu and L. C. Squire. An investigation of shock/boundary-layer interactions on curved surfaces at transonic speeds. *J. Fluid Mech*, 187:467–486, 1988.

[41] Xu-Dong Liu, Stanley Osher, and Tony Chan. Weighted essentially non-oscillatory schemes. *Journal of Computational Physics*, 115:200–212, 1994.

[42] P. Moin and J. Kim. Numerical investigation of turbulent channel flow. *J. Fluid Mech*, 118:341–377, 1982.

[43] M. Opiela, M. Meinke, and W. Schroder. LES of wake blade interaction in a turbine stage. In 9^{th} *International Symposium on Unsteady Aerodynamics, Aeroacoustics and Aeroelasticity of Turbomachines and First Legendre Lecture Series*, Lyon, 2000.

[44] J. Poggie and A. J. Smits. Shock unsteadiness in a reattaching shear layer. *J. Fluid Mech.*, 429:155–185, 2001.

[45] Y. G. Lai R. M. C. So, H. S. Zhang, and B. C. Hwang. Second order near wall turbulence closures : a review. *AIAA Journal*, 29(11):1819–1835, 1991.

[46] M. Sadeghi and F. Liu. Computation of cascade flutter with a coupled aerodynamic and structural model. In *ISUAAAT'2000 and First Legendre Lecture Series*, Lyon, 2000.

[47] A. Sergent, P. Joubert, P. Le Quéré, and C. Tenaud. Extension du modèle d'échelles mixtes à la diffusivité de sous-maille. *C. R. Acad. Sci. Paris*, 328, Serie II b:891–897, 2000.

[48] Chi-Wang Shu and Stanley Osher. Efficient implementation of essentially non-oscillatory shock-capturing schemes. *Journal of Computational Physics*, 77:439–471, 1988.

[49] P. R. Spalart. Strategies for turbulence modelling and simulations. *International Journal of Heat and Fluid Flow*, 21:252–263, 2000.

[50] C. Tenaud, E. Garnier, and P. Sagaut. Evaluation of some high-order shock capturing schemes for direct numerical simulation of unsteady two-dimensional free flow. *Int. Journal for Numerical Methods in Fluids*, 33:249–278, 2000.

[51] C. Tenaud and Loc Ta Phuoc. Large eddy simulation of unsteady, compressible, separated flow around NACA 0012 airfoil. In Monterey, editor, *15st ICNMFD*, CA, July 1996.

[52] Joe F. Thompson, Zahir U. A. Warsi, and C. Wayne Mastin. Boundary-fitted coordinate system for numerical solution of partial differential equations–a review. *Journal of Computational Physics*, 47:1–108, 1982.

[53] Kevin W. Thompson. Time dependent boundary conditions for hyperbolic systems. *Journal of Computational Physics*, 68:1–24, 1987.

[54] J. M. Verdon. Linearized Analysis of the Acoustic Response to Wake/Blade-Row Interaction. In *ISUAAAT'2000 and First Legendre Lecture Series*, Lyon, 2000.

[55] R. Verzicco, J. Mohd-Yusof, P. Orlandi, and D. Haworth. L. E. S. in complex geometries using boudary body forces. *Proceedings of the Summer Program, Center for Turbulence Research*, 1998.

[56] Bert Vreman, Bernard Geurts, and Hans Kuerten. A priori tests of large eddy simulation of the compressible plane mixing layer. *Journal of Engineering Mathematics*, 29:299–327, 1994.

[57] X. Wu and P. A. Durbin. Evidence of longitudinal vortices evolved from distorted wakes in a turbine passage. *J. Fluid Mech.*, 446:199–228, 2001.

[58] V. Yakhot and L. M. Smith. The renormalization group, the ϵ-expansion and derivation of turbulence models. *Journal of Scientific Computing*, 7:35–61, 1992.

[59] H. Yan and D. Knight. Large eddy simulation of supersonic compression corner using ENO scheme. In University of Texas, editor, *Third AFSOR Int. Conf. on DNS and LES*, Arlington, August 2001.